Journal of Environmental Chemical Engineering 5 (2017) 4742–4750

Contents lists available at ScienceDirect

Journal of Environmental Chemical Engineering

journal homepage: www.elsevier.com/locate/jece

Research paper

Raw montmorillonite modified with iron for photo-Fenton processes: influence of iron content on textural, structural and catalytic properties

María Andrea De León[a,*], Mayra Rodríguez[a], Sergio Gustavo Marchetti[b], Karim Sapag[c], Ricardo Faccio[d], Marta Sergio[a], Juan Bussi[a]

[a] Laboratorio de Fisicoquímica de Superficies, DETEMA, Facultad de Química, Universidad de la República, Gral. Flores 2124, CC 1157, CP 11800, Montevideo, Uruguay
[b] CINDECA, CONICET–Universidad Nacional de La Plata, Facultad de Ciencias Exactas, Calle 47 N 257, 1900, La Plata, Argentina
[c] Laboratorio de Sólidos Porosos, Instituto de Física Aplicada, CONICET, Universidad Nacional de San Luis, Chacabuco 917, CP 5700, San Luis, Argentina
[d] Cryssmat-Lab, DETEMA, Facultad de Química, Universidad de la República, Gral. Flores 2124, CC 1157, CP 11800, Montevideo, Uruguay

ARTICLE INFO

Keywords:
Fe-PILC
Iron content
Maghemite particles
Heterogeneous photo-Fenton
Phenol degradation

ABSTRACT

A raw montmorillonite was exchanged with the trinuclear Fe(III) acetate complex and calcined at 400 °C. Ratios of 0.5, 1.0 and 3.5 mmol of complex per gram of clay were employed. The pillared solids (Fe-PILCs) were analyzed by X-ray fluorescence spectroscopy, thermogravimetry analysis, scanning electron microscopy, Mössbauer spectroscopy, X-ray diffraction and nitrogen adsorption isotherms. Total iron amount incorporated by the clay increases with the complex/clay ratio used from 6.1% to 17.6%. Iron is incorporated mainly in the interlayer space when the clay is pillared with the smallest complex/clay ratio and a microporous network is generated. Adsorption of iron on the outer surface is favored for higher iron loads and results in the creation of a mesoporous structure. Mössbauer analysis shows the presence of iron as maghemite (γ-Fe_2O_3) particles with a wide particle size distribution. All the Fe-PILCs were active as catalysts for phenol degradation under photo-Fenton like conditions using UVA radiation and a maximum in their activity is achieved for an intermediate iron content (13.4%).

1. Introduction

Pillared clays (PILCs) constitute a family of materials displaying large specific surface area and micropore volume which are being studied as adsorbents and/or catalysts for several applications [1–5]. They are obtained by ion exchange of the interlayer cations of smectite-type clays by large metal polymeric species (pillaring agent) giving place to increased interlayer spacing, specific surface area and pore volume. The most common pillaring agents are bulky inorganic cations in the form of polynuclear oxocations, cationic metal complexes, metal clusters or positively charged colloidal particles of Al, Si, Ti and several transition metals (like Fe, Cr, Co, Mn and Ce). Moreover, synthesis conditions of the pillaring agent highly influence the size and charge of the metal species and thereby on the pore size and structure of the PILCs.

Iron pillared clays (Fe-PILCs) have attracted a special interest for their efficiency as catalysts in the elimination of organic pollutants from aqueous solutions by Fenton and photo-Fenton techniques [6–10]. Unlike the homogeneous systems, the Fe species involved in the reaction mechanism remain attached to the clay, allowing their recovering by simple separation procedures. Pillaring iron species are mainly obtained by partially hydrolyzed iron(III) solutions [11]. Iron polycations are then thermally decomposed leading to the formation of pillars between clay platelets and the increase of specific surface area. The trinuclear acetate iron(III) ions ($[Fe_3(OCOCH_3)_7OH]^+$) have also been used as pillar precursors leading to thermally stable materials even after heating up to 500 °C with interlayer spacing of 0.7 nm, gallery height of 0.84 nm and BET specific surface area of 284 $m^2\,g^{-1}$ [12–14]. Large iron(III) oxide particles along with the Fe_2O_3-pillared clays have been revealed by high-resolution transmission electron microscopy [12,15]. When catalysts prepared with this pillaring agent were tested in the photo-Fenton process, their activities were much higher than that of montmorillonites pillared with the traditional iron hydroxyl compound. Besides, the stability of the intercalated structure and the low leaching of iron suggest that these catalysts can be operated for a long time [16].

Considering these catalytic properties and the fact that these materials are cheap and reusable, more efforts to investigate their

* Corresponding author.
E-mail addresses: adeleon@fq.edu.uy (M.A. De León), m.rodriguezbennadji@gmail.com (M. Rodríguez), march@quimica.unlp.edu.ar (S.G. Marchetti), sapag@unsl.edu.ar (K. Sapag), rfaccio@fq.edu.uy (R. Faccio), msergio@fq.edu.uy (M. Sergio), jbussi@fq.edu.uy (J. Bussi).

http://dx.doi.org/10.1016/j.jece.2017.09.014
Received 20 May 2017; Received in revised form 9 August 2017; Accepted 8 September 2017
Available online 09 September 2017

physicochemical and catalytic properties could contribute to the design of an optimal preparation method as a part of strategies to develop their use in water treatment processes. In previous studies a natural montmorillonite without any further pre-treating than drying and grinding was pillared with the trinuclear acetate iron (III) ions. The influence of two operative variables of the PILC preparation method, the starting clay-mineral particle size and the final calcination temperature was analyzed [17–19]. These materials displayed catalytic activity in the degradation of dyes under photo-Fenton like conditions. In this sense, the present work reports the study of a series of Fe-PILCs prepared with the same montmorillonite clay and variable iron complex/clay ratios to obtain catalysts with different iron content. Emphasis is placed on the study of the influence of the iron content of the pillared materials on their structural properties and on their catalytic performance in phenol degradation under photo-Fenton like conditions.

2. Materials and methods

2.1. Clay

The raw clay, a highly pure montmorillonite, was extracted from Bañado de Medina (32° 23′ 0″ South, 54° 21′ 0″ West), Cerro Largo, Uruguay. Hydrogen peroxide test evidenced the absence of organic matter. Cation exchange capacity (CEC) of the clay, as determined by the ammonium acetate method (1 M and pH = 7), was 1.12 meq per gram of the dry clay. The solutions resulting from the CEC determination were analyzed by atomic absorption spectroscopy and atomic emission spectroscopy for the exchanged cations determination. The results in meq g^{-1} are as follows: Ca^{+2} 0.81; Mg^{+2} 0.29; Na^{+} 0.012; K^{+} 0.002 [20], accounting for the total CEC. The raw clay was oven dried at 105 °C for 24 h and ground. The fraction with aggregate size less than 250 μm, selected by sieving, is referred as Clay and was used for Fe-PILCs preparation.

2.2. Fe-PILCs preparation

The pillaring agent was the trinuclear acetate Fe(III) ion, $[Fe_3(OCOCH_3)_7OH{\cdot}2H_2O]^{+}$, that was prepared according to the method described by Yamanaka et al. [21]. A suspension of the clay in deionized water (10% in weight) was prepared to facilitate swelling and disaggregation. A solution of the iron complex in deionized water was poured slowly on the aqueous suspension of the clay until a complex/clay ratio of 0.5 mmol of the complex per gram of clay was attained. The resulting suspension was stirred for 3 h at 40 °C and then left for 21 h at room temperature. A part of the complex was not exchanged and remains in solution. The exchanged solid was recovered by vacuum filtration and repeatedly washed with deionized water until constant conductivity. The resulting solid was oven-dried at 60 °C and named as Fe-Ex-0.5. The exchanged sample was calcined in air atmosphere in a tubular furnace (Carbolite CTF-12/65/550); the temperature was increased at 1 °C min^{-1} up to 400 °C, which was maintained for 2 h. The obtained solid was named as Fe-PILC-0.5. This preparation method was repeated using 1.0 and 3.5 mmol of iron complex per gram of clay. The exchanged clays obtained were named as Fe-Ex-1.0 and Fe-Ex-3.5, and the iron pillared clays obtained after calcination as Fe-PILC-1.0 and Fe-PILC-3.5, respectively.

2.3. Characterization

The chemical composition of the solids was determined by energy dispersive X-ray fluorescence spectroscopy (EDXRF). SEM micrographs and EDS surface analysis were obtained with a JEOL JS M-5900LV scanning electron microscope operated at 20 kV. Thermogravimetric analysis (TGA) was performed in a Shimadzu TGA-50 equipment. Samples were heated in a platinum capsule up to 800 °C at a heating rate of 1 °C min^{-1}, at an air flow rate of 50 mL min^{-1}. Nitrogen adsorption-desorption isotherms were determined at −196 °C in a Micromeritics ASAP 2010 equipment. The samples were outgassed at 250 °C to a residual pressure lower than 10 mPa. The apparent specific surface area (S_{BET}) was determined by the BET model. The specific total pore volume (V_T) was obtained from the adsorbed amount at a relative pressure of 0.95 transformed to volume of liquid; a density of 0.808 mL g^{-1} for the adsorbed nitrogen was assumed. The specific micropore volume ($V_{\mu p}$) was determined by the Dubinin-Radushkevich model. The specific mesopore volume (V_{mp}) was determined as the difference between the specific total pore volume and the specific micropore volume. The powder X-ray diffraction data were obtained in a Rigaku Ultima IV, 285 mm radius, powder diffractometer operating in Bragg Brentano geometry using Cu Kα (0.15418 nm) radiation monochromatizated with a bent germanium crystal and using a scintillation detector. The data scanning in the 2θ degree range from 2°–70° in steps of Δ(2θ) = 0.02°, using fixed slits of ½°, in order to prevent beam spillage outside the 2 cm long sample, particularly for the measurement at very low angles, close to 2θ = 2°. Mössbauer spectra were obtained with a constant acceleration spectrometer with 512 channels, using transmission geometry and a nominal 50 mCi ^{57}Co source in a Rh matrix. Velocity speed calibration was performed with a 12 μm α-Fe film and isomer shifts values were referred to this standard. The spectra were evaluated using Recoil Spectral Analysis software [22].

2.4. Catalytic reactor

The reactor is composed of a borosilicate glass tube irradiated by four Philips TLD 18W/08 lamps place symmetrically around it (Fig. 1). The tube and the lamps are surrounded by an aluminium reflector sheet. The lamps emit UVA radiation between 340 nm and 420 nm (maximum emission at 360 nm). The reaction medium (0.5 L) is recirculated through the irradiated tube with a peristaltic pump. The reservoir is a jacketed vessel which is maintained at a constant temperature by recirculating water from a thermostated bath.

2.5. Catalytic tests

The catalytic activity of the catalysts was tested in the degradation of phenol under photo-Fenton-like conditions. The initial concentrations of phenol (C_6H_5OH) and hydrogen peroxide (H_2O_2) were respectively 0.2 mmol L^{-1} and 10 mmol L^{-1}. The catalyst (1.0 g L^{-1}) was maintained in suspension by magnetic stirring. The initial pH was adjusted to 3 with sulphuric acid and the temperature was at 30 °C. The reactant solution (0.2 mM in phenol and 10 mM in H_2O_2 at pH 3) were poured into the reactor. Once the desired temperature was attained, the catalyst was added and the light turned on.

2.6. Analytical methods

Samples of the reaction medium were withdrawn at several time intervals and filtered through 0.2 μm pore-size cellulose acetate membranes to separate the catalyst. The concentration of phenol and aromatic reaction intermediates (benzoquinone (BQ), hydroquinone (HQ) and catechol (Cat)) was determined by HPLC in a Shimadzu chromatograph equipped with a Nucleosil 100-5 C18 (Macherey-Nagel) column and UV detector. The eluent was a mixture of water/methanol/acetic acid (69:30:1) and the flow rate was 1.0 mL min^{-1}. Total organic carbon (TOC) was measured with a Sievers 800 analyser. Samples for total iron in solution determination were treated with ascorbic acid (reducing agent) to reduce Fe^{3+} to Fe^{2+} [23]. This allow all the iron in solution to be present as Fe^{2+}. Then total iron in the form of Fe^{2+} was determined by the colorimetric 1,10-phenantroline technique [24]. A Shimadzu UV–vis 1800 spectrophotometer was used for absorbance measurement of the Fe^{2+}-1,10-phenatroline complex at 510 nm (ε_{510} = 1.11 × 10^4 mol^{-1} L cm^{-1}).

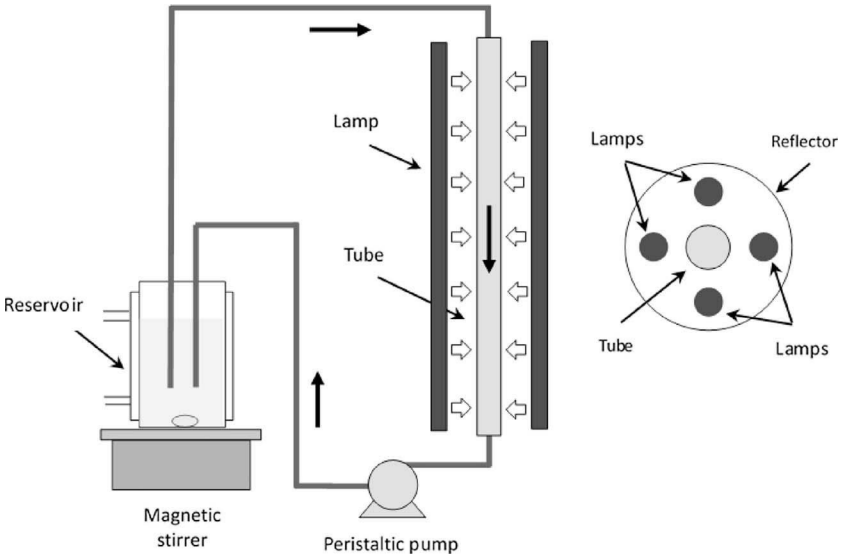

Fig. 1. Schematic diagram of the photo-reactor.

3. Result and discussion

3.1. EDXRF analysis

The composition of the host clay and the Fe-PILCs determined by EDXRF is presented in Table 1. The clay is rich in calcium and has a low content of sodium and potassium. Iron content of the clay is low (1.1%) and as it was not detected as exchangeable cation [20] it is included in the clay layers substituting either Al or Si. Increasing amounts of iron (6.1%, 13.4% and 17.6%) were incorporated in the Fe-PILCs along with the increase of the complex/clay ratio used in their preparation, meanwhile Ca^{2+} content diminishes. These results show the exchangeable nature of calcium ions and the effectiveness of the pillaring process. Potassium content for all samples is practically constant (considering dilution produced during the pillaring process), showing that this ion is not exchangeable. Fig. 2 shows the amount of incorporated iron vs. the complex/clay ratio used in the Fe-PILCs preparation. An approximately linear relationship between the iron incorporated and the complex/clay ratio is observed for Fe-PILC-0.5 and Fe-PILC-1.0. However, the linearity does not tally for Fe-PILC-3.5. The deviation from linearity for higher complex/clay ratios is typical of adsorption and ion exchange processes in which a limited number of adsorption and/or exchange sites are present in the solid, as in the case of the montmorillonite here used.

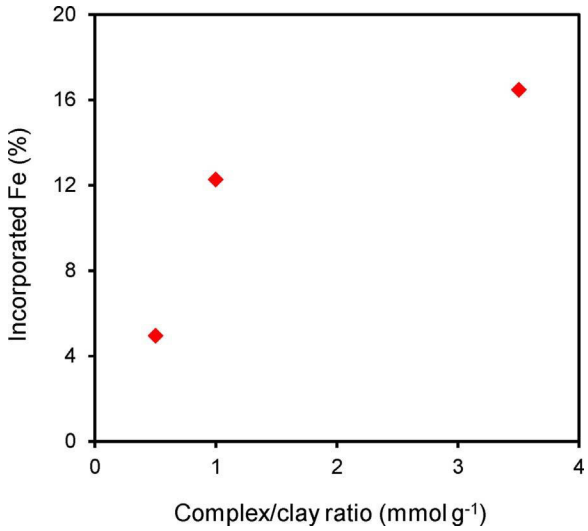

Fig. 2. Incorporated Fe as a function of the complex/clay ratio used in the preparation of the catalysts.

Table 1
Chemical composition of the clay and Fe-PILCs determined by EDXRF.

Element	Solid			
	Clay	Fe-PILC-0.5	Fe-PILC-1.0	Fe-PILC-3.5
Na (ppm)	< LD[a]	< LD[a]	< LD[a]	< LD[a]
Mg (wt%)	< 2	< 2	< 2	< 2
Al (wt%)	7.9	4.5	4.5	6.6
Si (wt%)	31	25	24	28
K (wt%)	0.14	0.11	0.11	0.11
Ca (wt%)	1.38	0.96	0.19	< LD[b]
Ti (ppm)	542	844	838	666
Mn (ppm)	1610	1832	1708	1259
Fe (wt%)	1.1	6.1	13.4	17.6
Cu (ppm)	6.1	8.6	8.4	8.7
Zn (ppm)	117	122	110	83
Rb (ppm)	7	7.1	3.4	< LD[c]
Sr (ppm)	257	172	42	5.8
Pb (ppm)	30	33	24	14

[a] LD_{Na} = 100 ppm.
[b] LD_{Ca} = 50 ppm.
[c] LD_{Rb} = 0.5 ppm.

Fig. 2 suggests a maximum amount of iron that can be incorporated by pillaring. This maximum value should be related to the clay CEC and suggests that the ionic exchange mechanism plays a key role for iron incorporation in the clay. Trinuclear acetate iron complex/clay ratios over 5 are reported by Yamanaka et al. [21] as necessary to attain total ion exchange of the clay. Nevertheless, partial iron incorporation by adsorption cannot be ruled out according to the work of Martin-Luengo et al. [13].

3.2. Scanning electron microscopy

The scanning electron micrographs of the host clay and the Fe-PILCs are shown in Fig. 3. The lamellar and ordered structure characteristic of montmorillonite is clearly observed in Fig. 3a. It is observed that the particles are irregular platelets and stacked on top of each other to form a variety of aggregates with different sizes and thicknesses. The image shows a dominant flake-like morphology and irregular edges, where only interparticle pores are appreciated. Fig. 3b–d shows the SEM images of the Fe-PILCs where the modification of the clay structure by the iron pillaring process can be observed. The swelling and increased

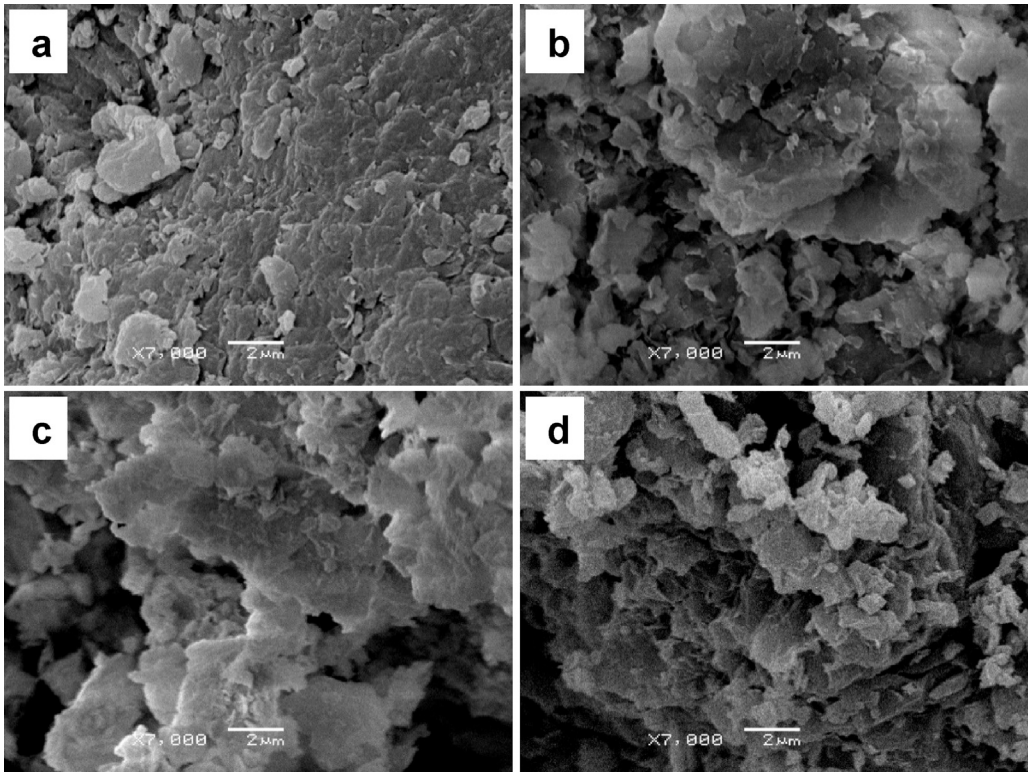

Fig. 3. SEM images of the clay and the Fe-PILCs: (a) the host clay (b) Fe-PILC-0.5 (c) Fe-PILC-1.0 and (d) Fe-PILC-3.5.

structural disorder is appreciated although typical layered structure of montmorillonites was partially retained. These solids have a porous spongy appearance that Zeng et al. [25] describe as "corn flakes" and endorsed to the micropores increase associated with the intercalation of iron oxide pillars into the interlayer space of the clay. The images show that Fe-PILCs are constituted by randomly oriented irregular shape aggregates with different particle sizes that causes a highly heterogeneous internal structure.

Fig. 4 shows the iron content determined by EDS at six different sites on the surface of the Fe-PILCs. For each solid, iron content varies significantly according to the selected site, showing that the pillaring procces produce a non-homogeneous iron content on the surface. The range of these values for Fe-PILC-0.5 includes the total iron content determined by EDXRF (Table 1), for Fe-PILC-1.0 the majority of these values are higher than the EDXRF one, while for Fe-PILC-3.5 all of them exceed that obtained by EDXRF. According to these results, the amount of iron found on the surface of the Fe-PILCs increases with the complex/clay ratio used in their preparation, thus showing that not all the iron species have been included as pillars in the interlayer space. Mishra et al. [12] report that using the trinuclear complex for pillaring a montmorillonite, a part of the complex is adsorbed on the surface instead of introducing inside the clay interlayer spaces. Marco-Brown et al. [26] found that the pillaring process of a sodic montmorillonite with polycations obtained by basic hydrolysis of iron salts drastically increases the iron content in the outer surface of the clay.

Calcium at different points of the surface of the clay and the Fe-PILCs was also determined by EDS. The average values were: 1.55% for the clay, 0.83% for Fe-PILC-0.5, 0.20% for Fe-PILC-1.0 and calcium was not detected in Fe-PILC-3.5. The results show the same decreasing tendency along with the increase of iron content, thus confirming that the exchange between calcium and the iron complex took place during the pillaring process.

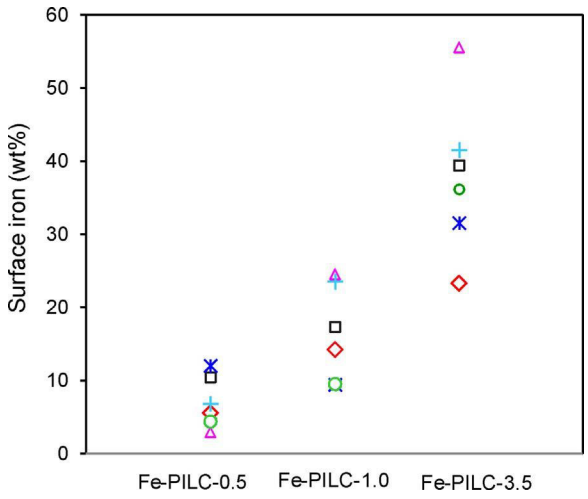

Fig. 4. Iron content at different sites of the Fe-PILCs surfaces determined by EDS.

3.3. Thermal analysis

The thermogram (TGA) and the derivative thermogravimetric analysis (DrTGA) for the clay are presented in Fig. 5a. A significant mass loss (14.7%) between room temperature and 150 °C is observed and attributed to water that is either physisorbed on the surface of the clay or associated to exchangeable cations in the interlayer space. At higher temperature, between 540 °C and 670 °C, a peak in the derivative curve evidences a second mass loss attributed to the dehydroxylation of the montmorillonite.

Fig. 5b shows the TGA and the DrTGA analysis for Fe-Ex-3.5, the solid obtained with the higher complex/clay ratio. The mass loss observed between room temperature and 155 °C (13%) is assigned to water desorption. Another mass loss between 214 °C and 339 °C (4.1%) is attributed to the decomposition and oxidation of the acetate groups of the iron complex [21,27] incorporated during the ion exchange and is related to the formation of iron oxide pillars between the clay sheets. The slight variation observed in the DrTGA in the vicinity of 540 °C is ascribed to the dehydroxylation of montmorillonite. The TGA and

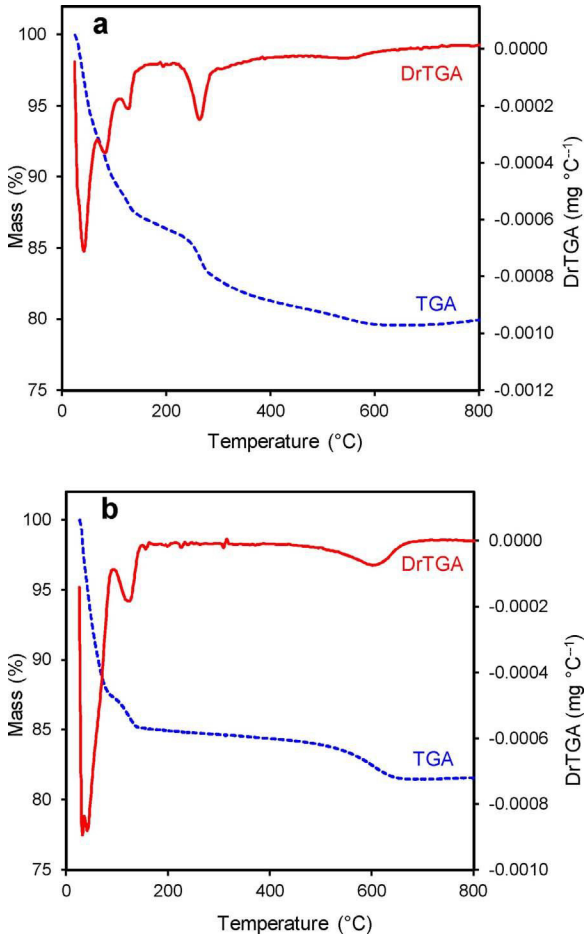

Fig. 5. Thermogravimetric analysis for: (a) host clay and (b) Fe-Ex-3.5.

Table 2
Thermogravimetric analysis: identification of mass loss processes for Fe-Ex-0.5, Fe-Ex-1.0, Fe-Ex-3.5.

Process		Exchange clay		
		Fe-Ex-0.5	Fe-Ex-1.0	Fe-Ex-3.5
Water loss	Temperature range (°C)	T_{amb}–150	T_{amb}–154	T_{amb}–155
	Mass loss (%)	16.3	13.4	12.9
Complex decomposition	Temperature range (°C)	214–328	215–349	214–339
	Mass loss (%)	0.85	2.88	4.11

DrTGA profiles for Fe-Ex-1.0 and Fe-Ex-0.5 are like those described for Fe-Ex-3.5 (Fig. 5b) although smaller variations in the mass losses are observed. Table 2 summarizes this information for the three exchanged clays. It can be seen that the mass loss attributed to the complex decomposition increases with the complex/clay ratio used in the exchange indicating an increase in the iron complex amount incorporated into the clay. TGA results confirm that at 400 °C, calcination temperature of the exchanged clays, the iron complex decomposition is complete.

3.4. XRD analysis

X-ray diffraction pattern for the raw clay is shown in Fig. 6. The sharp peak at 2θ = 5.84° corresponds to the d_{001} basal spacing of 1.51 nm that is typical of calcium-rich montmorillonites and is in accordance with EDXRF data (Table 1). The peak about 2θ = 20° and the broad one nearby 2θ = 35° are characteristic for smectites (JCPDS Card # 13–135), as well as others indicated in Fig. 6. Those observed at 2θ = 26.66° and 2θ = 20.88° are assigned to quartz impurities (JCPDS Card # 78–1253).

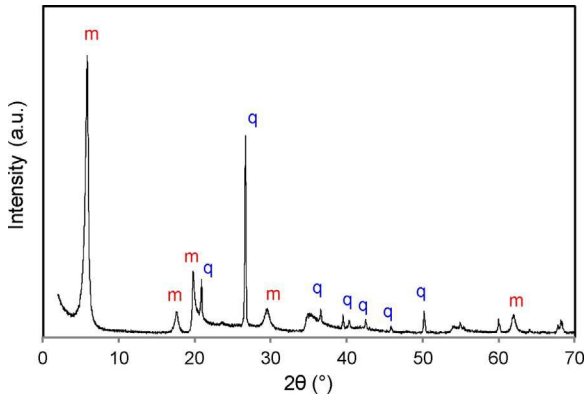

Fig. 6. XRD pattern for the host clay. m: montmorillonite, q: quartz.

In order to evaluate the pillaring process efficiency, X-ray diffraction patterns up to 2θ = 12° for the exchanged clays and the Fe-PILCs are presented in Fig. 7. A well-defined peak at 2θ = 5.82° is observed for Fe-Ex-0.5 (Fig. 7a) and corresponds to a basal spacing of 1.52 nm. A less intense and broad peak between 2θ = 5.78° and 5.92° (centered at 5.82) for Fe-PILC-0.5 is also clearly depicted (Fig. 7b). According to these results, thermally stable d_{001} spacing with gallery heights of 0.53 nm was attained after the pillaring process. While the peak at 2θ = 5.82° is clearly defined for Fe-PILC-0.5, only a broad shoulder is observed for Fe-PILC-1.0 and for Fe-PILC-3.5 is not observed. Another broad shoulder centered at around 2θ = 8° is observed for these catalysts (Fig. 7b) and is ascribed to a little fraction of the clay that remains unpillared [28,29]. For this fraction, a decrease of the basal spacing to about 1.1 nm took place during the pillaring process.

These results clearly show the loss of crystallinity that take place along with the increase of iron content. Maes and Vansant [30] reported the loss of crystallinity for high iron contents working with the same iron complex. Nevertheless, Yamanaka et al. [21] reported the presence of crystallinity in Fe-PILCs containing iron amounts as high as 25%. It is worth to note that comparison of results reported by different authors is not possible because, even if the same starting clay is used, they are influenced by the history of the sample (the particle sized fraction and/or the type of homoionic form used for pillaring) as well as many other preparation parameters that are often not completely described.

3.5. Textural analysis

Nitrogen adsorption isotherms for the Fe-PILCs and the host clay are shown in Fig. 8. The clay exhibits a Type II isotherm and a type H4 hysteresis cycle, characteristic of the presence of narrow pores [31] among the flat particles of montmorillonite, as seen in the micrograph (Fig. 3a).

Isotherms of Fe-PILCs show significant adsorption at low relative pressures (Type I isotherm) indicating the presence of micropores and a small hysteresis cycle indicative of mesopores (Type IV isotherm). The hysteresis cycle is type H3 [31], which is characteristic of flat particles aggregates, such as the solids here studied. The amount of nitrogen adsorbed at low relative pressures increases along with the complex/clay ratio used during the pillaring process and it is mainly related to the increasing microporous network derived from the inclusion of more pillars in the interlayer space of the host clay. It is worth to note that adsorption isotherm branches for Fe-PILC-0.5 and Fe-PILC-1.0 are parallel to that of the host clay in the range of intermediate relative pressures, which indicates that the interparticle porosity underwent little change and the main structural difference among them is the

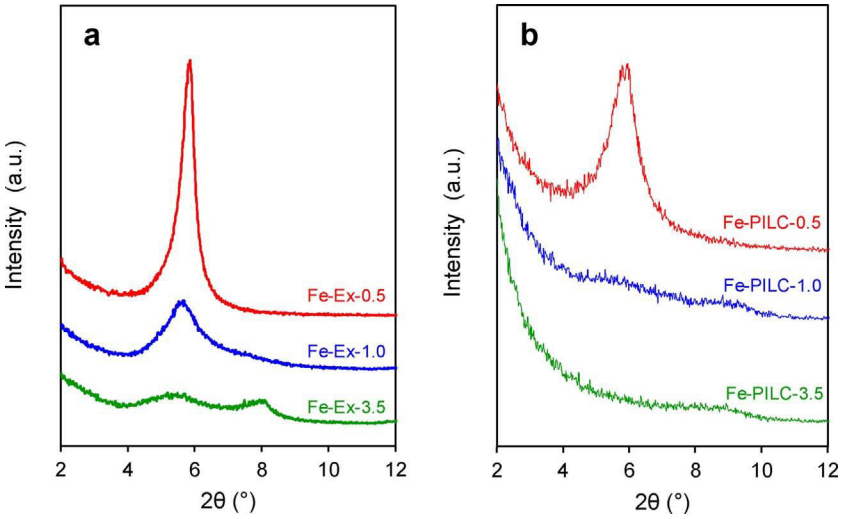

Fig. 7. XRD patterns for the solids: (a) exchanged clays and (b) Fe-PILCs.

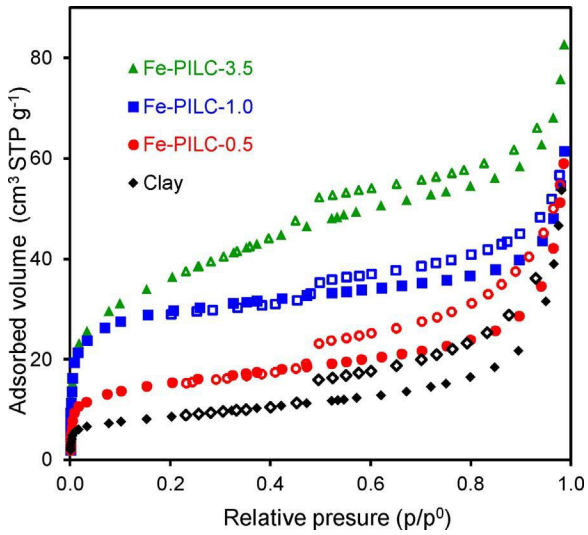

Fig. 8. Nitrogen adsorption-desorption isotherms for the clay and the Fe-PILCs. Filled symbols: adsorption, empty symbols: desorption.

development of the microporous structure [32]. On the contrary, the Fe-PILC-3.5 isotherm displays a higher slope which indicates the increase of the interparticle porosity corresponding to mesopores [32].

Table 3 shows the textural parameters derived from nitrogen adsorption isotherms for the clay and the Fe-PILCs. Specific surface area (S_{BET}), specific micropore volume ($V_{\mu p}$) and total pore volume increase along with iron content and for Fe-PILC-3.5 attain values of 130 $m^2 g^{-1}$, 0.52 $cm^3 g^{-1}$ and 0.099 $cm^3 g^{-1}$, respectively. The higher mesopore volume for Fe-PILC-3.5 is coincident with the steeper slope of the isotherm in the range of intermediate pressures.

According to textural properties here reported, when the clay is pillared with the lowest complex/clay ratio (Fe-PILC-0.5), iron is incorporated mainly in the interlayer space producing a microporous network and causing a significant increase of the micropore volume and specific surface area regarding the host clay. A higher amount of iron incorporated in Fe-PILC-1.0 increases the specific surface area and the micropore volume because of the incorporation of larger amounts of iron in the interlayer space. A slight decrease of the mesopore volume would be associated to the complex adsorption in the interparticle space. At greater iron contents (Fe-PILC-3.5) a pronounced increase in the volume of mesopores takes place while the micropore volume increases slightly. This fact suggests that just a small proportion of the extra iron has been incorporated into the interlayer space of the Fe-PILC-3.5. In this regard, Yuan et al. [33] proposed that part of the added iron is agglomerated outside the interlayer space, on the outer surface of the aggregates, being responsible for the loss of long-range structural order as it was shown in XRD results and leading to the delamination of the pillared clay.

Table 3
Textural parameters derived from nitrogen adsorption isotherms for the clay and the Fe-PILCs.

Solid	S_{BET} ($m^2 g^{-1}$)	V_T ($cm^3 g^{-1}$)	$V_{\mu p}$ ($cm^3 g^{-1}$)	V_{mp} ($cm^3 g^{-1}$)
Clay	31	0.049	0.013	0.036
Fe-PILC-0.5	56	0.057	0.023	0.034
Fe-PILC-1.0	111	0.069	0.046	0.023
Fe-PILC-3.5	130	0.099	0.052	0.047

3.6. Mössbauer spectroscopy

Mössbauer spectra for the clay and the Fe-PILCs obtained at 25 °C are presented in Fig. 9 and the corresponding hyperfine parameters are shown in Table 4. The spectra for all samples only display one doublet with an isomer shift (δ) of 0.34–0.35 mm s^{-1}, characteristic of high spin Fe^{3+} ions. The quadrupole splitting (Δ) increases from 0.57 mm s^{-1} for the clay to values in the range 0.73–0.76 mm s^{-1} for the pillared samples, suggesting a higher symmetry for the Fe^{3+} ions sites in the clay [34].

Fig. 10 shows the Mössbauer spectrum for Fe-PILC-3.5 at −211 °C. This spectrum was fitted with two sextuplets without magnetic relaxation, one relaxing sextuplet and a doublet. The corresponding hyperfine Mössbauer parameters are presented in Table 5. Considering these values, the two non-relaxing sextuplets can be assigned to Fe^{3+} ions located in tetrahedral and octahedral sites of the cubic spinel of maghemite (γ-Fe_2O_3) nanoparticles [34]. The magnetic hyperfine fields (H) of both sites are decreased with respect to bulk values [34]. This can be assigned to the phenomenon of collective magnetic excitations observed for very small particles at temperatures below that for its magnetic blocking [35]. The relaxing fraction would correspond to smaller nanoparticles of the same species (γ-Fe_2O_3) that have not completed their magnetic blocking at this temperature. According to these results, particle size distribution of γ-Fe_2O_3 in Fe-PILC-3.5 must be broad because otherwise all particles would block magnetically in a complete way in a very narrow temperature range. Smaller particles must be associated with those forming pillars, while the larger ones correspond to those located in the interparticles. The central doublet of the spectrum corresponds to paramagnetic Fe^{3+} ions. It is worth to note

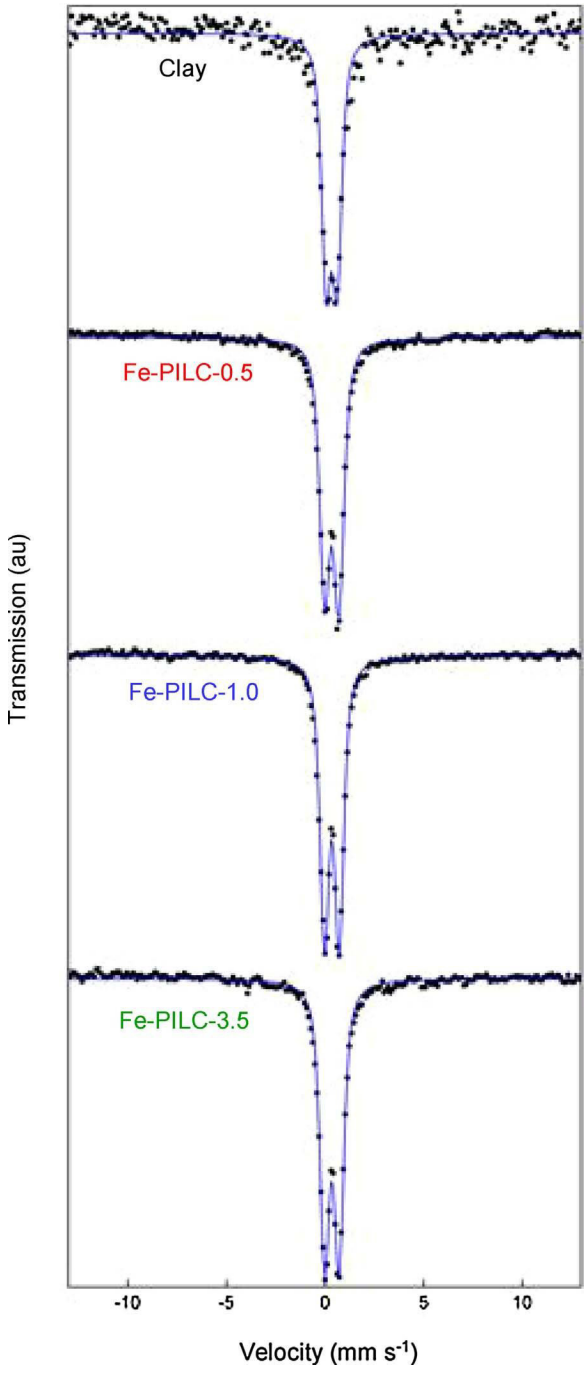

Fig. 9. Mössbauer spectra for the clay and the Fe-PILCs at 25 °C.

Table 4
Hyperfine Mössbauer parameters at 25 °C for the clay and the Fe-PILCs.

	Hyperfine Mössbauer parameters	
	Δ (mm s^{-1})	δ (mm s^{-1})
Clay	0.57 ± 0.02	0.34 ± 0.02
Fe-PILC-0.5	0.74 ± 0.01	0.35 ± 0.01
Fe-PILC-1.0	0.76 ± 0.01	0.35 ± 0.01
Fe-PILC-3.5	0.73 ± 0.01	0.34 ± 0.01

Δ: quadrupole splitting; δ: isomer shift.

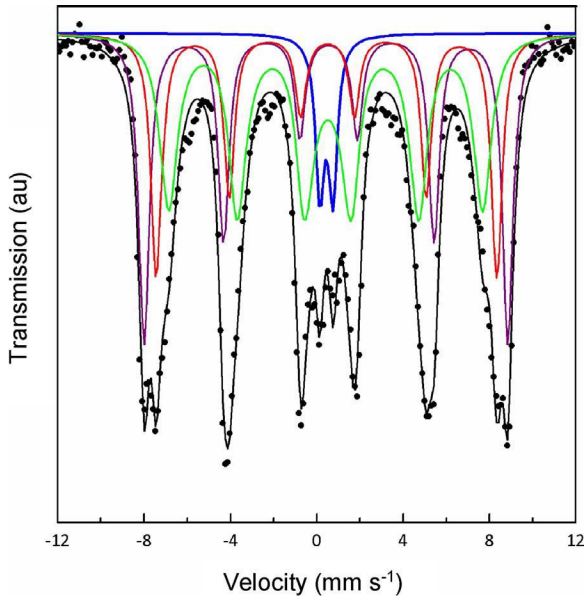

Fig. 10. Mössbauer spectra for Fe-PILC-3.5 at −261 °C.

Table 5
Hyperfine Mössbauer parameters at −261 °C for Fe-PILC-3.5.

Species	Hyperfine Mössbauer parameters	
γ-Fe_2O_3 tetrahedral site	H (T)	48.9 ± 0.1
	δ (mm s^{-1})	0.48 ± 0.01
	2ε (mm s^{-1})	−0.05 ± 0.02
	%	23 ± 2
γ-Fe_2O_3 octahedral sites	H (T)	52.23 ± 0.08
	δ (mm s^{-1})	0.49 ± 0.01
	2ε (mm s^{-1})	−0.12 ± 0.02
	%	30 ± 1
γ-Fe_2O_3 relaxing fraction	H (T)	45.2 ± 0.2
	δ (mm s^{-1})	0.46 ± 0.02
	2ε (mm s^{-1})	−0.11 ± 0.03
	%	41 ± 3
paramagnetic Fe^{3+}	Δ (mm s^{-1})	0.61 ± 0.04
	δ (mm s^{-1})	0.45 ± 0.02
	%	6 ± 1

H: hyperfine magnetic field; δ: isomer shift (values referred to α-Fe at 25 °C); 2ε: quadrupole shift; Δ: quadrupole splitting.

that at this temperature the quadrupolar splitting (0.61 ± 0.04 mm s^{-1}) is identical to that for the clay (0.57 ± 0.02 mm s^{-1}). Therefore, it can be proposed that the doublet for the Fe-PILC-3.5 at 25 °C is composed by the contribution of two doublets: one of them corresponds to Fe^{3+} ions initially present in the host clay network and the other, with a larger value of Δ, assigned to the superparamagnetic γ-Fe_2O_3 nanoparticles introduced during the pillaring process.

3.7. Catalytic tests

Fig. 11a shows the time-course of phenol concentration in solution during the degradation tests under photo-Fenton like conditions. The curve profile for Fe-PILC-0.5 exhibited an induction period with a small decrease of phenol concentration (5%) in the first 60 min of reaction and total phenol degradation after 180 min. This induction period is probably related with the surface activation of iron species [36] and with phenol adsorption on the catalyst surface [36,37]. Fe-PILC-1.0 (with an iron content of 13.4%) showed a better performance than Fe-PILC-0.5, reaching total phenol degradation after 60 min of reaction. These results suggest an increasing reaction rate along with the increase

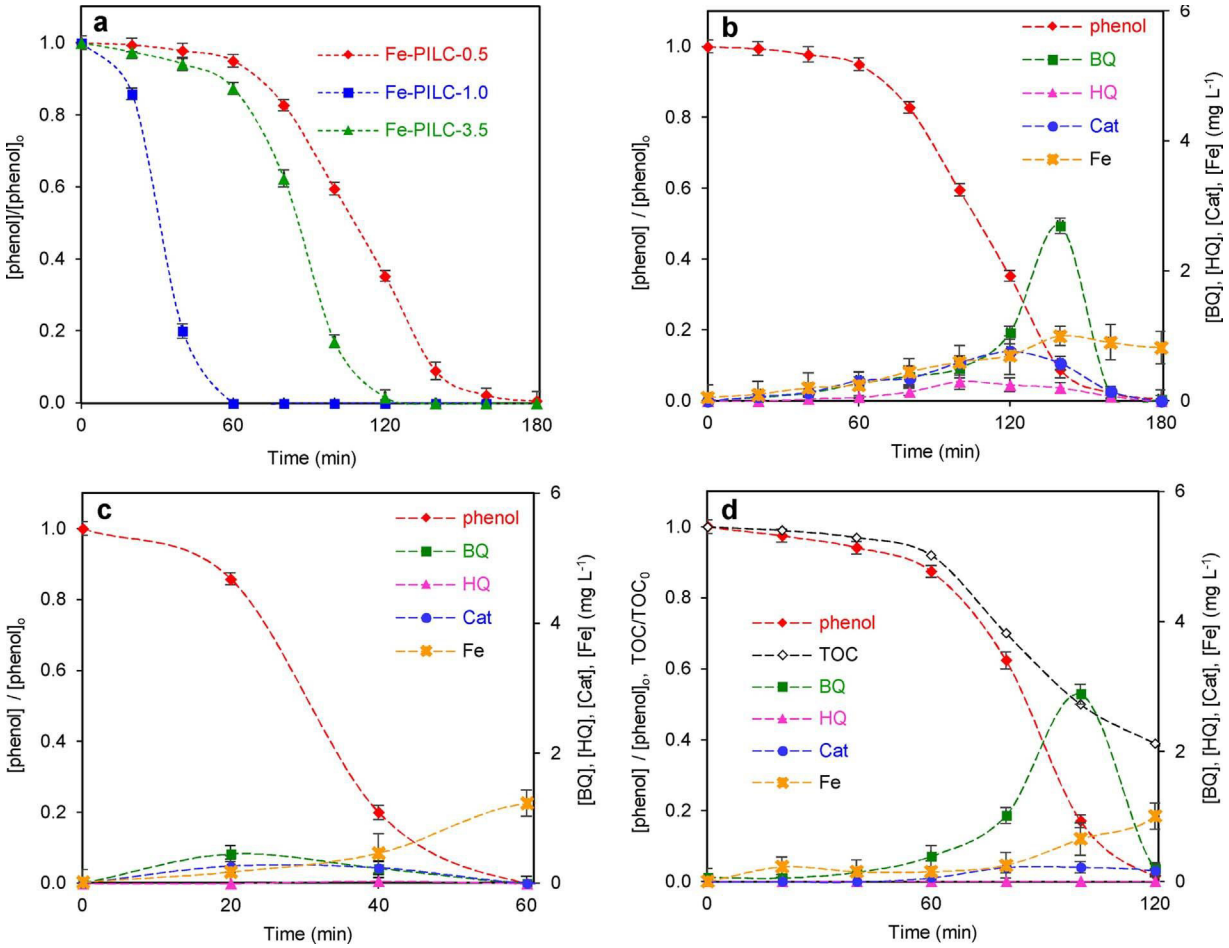

Fig. 11. Phenol degradation tests by photo-Fenton process using Fe-PILCs as catalyst. (a) dimensionless concentration of phenol in solution for the Fe-PILCs. Concentration of benzoquinone (BQ), hydroquinone (HQ), catechol (Cat) and total iron in solution (Fe) for: (b) Fe-PILC-0.5, (c) Fe-PILC-1.0 and (d) Fe-PILC-3.5, including total organic carbon (TOC).

of iron content of the catalyst. However, the catalyst with the highest iron content (Fe-PILC-3.5) deviates from this trend. Total phenol degradation was achieved in a larger reaction time (120 min) and the induction period was 40 min for a phenol degradation of 6%. The clay in its natural form were tested as catalyst in the photo-Fenton process using the same experimental conditions used for Fe-PILCs. The solid does not show catalytic activity in phenol degradation so its contribution to the catalytic activity of Fe-PILCs can be discarded. These results show that, besides the iron content, other textural and structural properties of Fe-PILCs affect their catalytic activity. Probably, surface accumulation of maghemite nanoparticles in the Fe-PILC-3.5 catalyst hinders reagents access to the microporous structure where the iron oxide pillars are placed.

According to these results, the Fe-PILC-1.0 with an intermediate value of iron content showed the best catalytic performance for phenol degradation. In order to compare with literature results, total phenol degradation is reported to be achieved in a larger reaction time (90 min), using an iron pillared laponite with higher iron content (21%) than Fe-PILC-1.0 (13.4%), a lower initial phenol concentration (0.1 mmol L^{-1}) and a higher H_2O_2 concentration (50 mmol L^{-1}) [38]. These results set a promising performance of Fe-PILCs here studied as catalysts in heterogeneous photo-Fenton processes.

Fig. 11b–d shows the evolution of the main reaction intermediates formed in the phenol degradation, benzoquinone (BQ), hydroquinone (HQ) and catechol (Cat) [39], as well as total iron in solution (Fe) for each catalyst separately. For Fe-PILC-0.5 (Fig. 11b), aromatic intermediates are totally degraded at 180 min of reaction and BQ is the one that reaches the highest concentration, 2.7 mg L^{-1} at 140 min. For Fe-PILC-1.0, the catalyst that showed the best performance in phenol degradation, only the presence of BQ and Cat are observed and its total degradation is achieved in only 60 min, with a maximum BQ concentration of 0.5 mg L^{-1} (Fig. 11c). This shows the higher efficiency of this catalyst not only to degrade phenol but also in the degradation of the aromatic intermediates.

In order to evaluate the extent of phenol mineralization, TOC results for the catalytic test with Fe-PILC-3.5 are included in Fig. 11d. The TOC removal profile shows that TOC in solution decreases and attains 39% at the end of the assay. Beside the aromatic intermediates (BQ, HQ, Cat), short-chain organic acids such as acetic, oxalic, maleic and formic acids are reported as reaction intermediate [40]. Although their degradation is possible, oxalic and acetic acid appeared to be refractory to this oxidation treatment [40] and could be responsible for the remaining TOC here observed.

Iron leaching is observed for all the Fe-PILCs (Fig. 11b–d). The maximum iron concentration detected is only 1.3 mg L^{-1} which is like those reported for other iron-pillared clay used in photo-Fenton processes [41,42]. It is worth to note that the amount of iron leached by the catalysts at the end of the tests represents only 1.7% for Fe-PILC-0.5, 0.9% for Fe-PILC-1.0 and 0.6% for Fe-PILC-3.5. This shows a great stability of these catalysts against the loss of the active phase, so it would be feasible to reuse them in the catalytic process for several cycles before rejecting or restoring its catalytic activity.

4. Conclusions

Iron oxide-pillared structures with a total iron content between

6.1% and 17.6% were obtained starting from a raw Uruguayan montmorillonite clay using trinuclear Fe(III) acetate complex/clay ratios between 0.5 and 3.5 mmol g^{-1}. The lamellar structure of the clay is progressively disordered along with the increase of its total iron content leading to delamination. Iron was incorporated as nanoparticles of maghemite (γ-Fe_2O_3) with a wide particle size distribution. The specific surface area and the micropore volume are much higher than those of the clay. When pillaring the clay with the smallest complex/clay ratio (0.5 mmol g^{-1}), iron is incorporated mainly in the interlayer space and a microporous network is generated. The increase of total iron content along with the complex/clay ratio leads to an increased iron adsorption on the outer surface of clay particles generating a mesoporous structure.

The Fe-PILCs were effective as catalysts for phenol and aromatic intermediates degradation under photo-Fenton like conditions. The differences in their catalytic behaviour not only depend on the total iron content but also on their textural and structural properties. Fe-PILC-1.0 with an iron content of 13.4% showed the best catalytic performance. In addition, the catalysts could retain the iron incorporated in their preparation since a low iron leaching was observed.

Acknowledgements

The authors thank Laboratorio de Tecnogestión of the Ministerio de Industria, Energía y Minería of Uruguay for the EDXRF analysis. This research was funded by Comisión Sectorial de Investigación Científica (CSIC), Universidad de la República and Programa de Desarrollo de las Ciencias Básicas (PEDECIBA).

References

[1] A. Gil, S.A. Korili, R. Trujillano, M.A. Vicente, Pillared Clays Related Catalysts, Springer, New York, 2010.
[2] Z. Ding, T.J. Kloprogge, R.L. Frost, G.Q. Lu, H.Y. Zhu, Porous clays and pillared clays-based catalysts. Part 2: a review of the catalytic and molecular sieve applications, J. Porous Mater. 8 (2001) 273–293.
[3] S. Barreca, J.J.V. Colmenares, A. Pace, S. Orecchio, C. Pulgarin, *Escherichia coli* inactivation by neutral solar heterogeneous photo-Fenton (HPF) over hybrid iron/montmorillonite/alginate beads, J. Environ. Chem. Eng. 3 (2015) 317–324.
[4] S. Barreca, S. Orecchio, A. Pace, The effect of montmorillonite clay in alginate gel beads for polychlorinated biphenyl adsorption: isothermal and kinetic studies, Appl. Clay Sci. 99 (2014) 220–228.
[5] L.F. González-Bahamón, D.F. Hoyos, N. Benítez, C. Pulgarín, New Fe-immobilized natural bentonite plate used as photo-Fenton catalyst for organic pollutant degradation, Chemosphere 82 (2011) 1185–1189.
[6] H.B. Hadjltaief, M.B. Zina, M.E. Galvez, P. Da Costa, Photo-Fenton oxidation of phenol over a Cu-doped Fe-pillared clay, C. R. Chimie 18 (2015) 1161–1169.
[7] E. Martin del Campo, R. Romero, G. Roa, E. Peralta-Reyes, J. Espino-Valencia, R. Natividad, Photo-Fenton oxidation of phenolic compounds catalyzed by iron-PILC, Fuel 138 (2014) 149–155.
[8] T. Xu, Y. Liu, F. Ge, Y. Ouyang, Simulated solar light photooxidation of azocarmine B over hydroxyl iron-aluminium pillared bentonite using hydrogen peroxide, Appl. Clay Sci. 100 (2014) 35–42.
[9] J. Herney-Ramirez, M.A. Vicente, L.M. Madeira, Heterogeneous photo-Fenton oxidation with pillared clay-based catalysts for wastewater treatment: a review, Appl. Catal. B Environ. 98 (2010) 10–26.
[10] S. Barreca, J.J.V. Colmenares, A. Pace, S. Orecchio, C. Pulgarin, Neutral solar photo-Fenton degradation of 4-nitrophenol on iron-enriched hybrid montmorillonite-alginate beads (Fe-MABs), J. Photochem. Photobiol. A: Chem. 282 (2014) 33–40.
[11] J.T. Kloprogge, Synthesis of smectites and porous pillared clays catalysts: a review, J. Porous Mat. 5 (1998) 5–41.
[12] T. Mishra, K.M. Parida, S.B. Rao, Transition metal oxide pillared clay: 1. A comparative study of textural and acidic properties of Fe(III) pillared montmorillonite and pillared acid activated montmorillonite, J. Colloid Interf. Sci. 183 (1996) 176–183.
[13] M.A. Martín-Luengo, H. Martins-Carvalho, J. Ladriere, P. Grange, Fe(III)-pillared montmorillonites: preparation and characterization, Clays Miner 24 (1989) 495–504.
[14] S. Yamanaka, M. Hattori, Iron oxide pillared clay, Catal. Today 2 (1988) 261–270.
[15] H. Mori, H. Miyoshi, K. Takeda, H. Yoneyama, H. Fujita, Y. Iwata, Y. Otsuka, Y. Muratu, TEM observation of iron oxide pillars in montmorillonite, J. Mater. Sci. 27 (1992) 3197–3199.
[16] S. Zhang, S. Liang, X. Wang, J. Long, Z. Li, L. Wu, Trinuclear iron cluster intercalated montmorillonite catalyst: microstructure and photo-Fenton performance, Catal. Today 175 (2011) 362–369.
[17] M.A. De León, M. Sergio, J. Bussi, Iron-pillared clays as catalysts for dye removal by the heterogeneous photo-Fenton technique, React. Kinet. Mech. Cat. 110 (2013) 101–117.
[18] M.A. De León, M. Sergio, J. Bussi, G.B. Ortiz de la Plata, A.E. Cassano, O.M. Alfano, Application of a montmorillonite clay modified with iron in photo-Fenton process. Comparison with goethite and nZVI, Environ. Sci. Pollut. Res. 22 (2015) 864–869.
[19] M.A. De León, J. Castiglioni, J. Bussi, M. Sergio, Catalytic activity of an iron pillared montmorillonite clay mineral in a heterogeneous photo-Fenton process, Catal. Today. 133–135 (2008) 600–605.
[20] M. Sergio, S. Cardozo, C. Froche, M. Bentancor, M. Musso, W. Diano, In A Clay Odyssey, in: E.A. Domínguez, G.R. DMs, F. Cravero (Eds.), Elsevier, Nederland, 2003, pp. 639–646.
[21] S. Yamanaka, T. Doi, S. Sako, M. Hattori, High surface area solids obtained by intercalation of iron oxide pillars in montmorillonite, Mater. Res. Bull. 19 (1984) 161–168.
[22] K. Lagarec, D.G. Rancourt, Mossbauer Spectral Analysis Software, Version 1.0, Department of Physics, University of Ottawa, 1998.
[23] J. Farias, E.D. Albizzati, O.M. Alfano, Kinetic study of the photo-Fenton degradation of formic acid. Combined effects of temperature and iron concentration, Catal. Today 144 (2009) 117–123.
[24] APHA, AWWA, WEF, Standard Methods for the Examination of Water and Wastewater, 21st ed., APHA-AWWA-WEF, Washington, D.C, 2005.
[25] L. Zeng, S. Wang, X. Peng, J. Geng, C. Chen, M. Li, Al-Fe PILC preparation, characterization and its potential adsorption capacity for aflatoxin B1, Appl. Clay Sci. 83–84 (2013) 231–237.
[26] J.L. Marco-Brown, C.M. Barbosa-Lema, R.M. Torres Sánchez, R.C. Mercader, M. dos Santos Alfonso, Adsorption of picloram herbicide on iron oxide pillared montmorillonite, Appl. Clay Sci. 58 (2012) 25–33.
[27] K.M. Parida, T. Mishra, D. Das, S.N. Chintalpudi, Thermal transformation of trinuclear Fe III acetate/complex intercalated montmorillonite, Appl. Clay Sci. 15 (1999) 463–475.
[28] P. Cañizares, J.L. Valverde, M.R. Sun Kou, C.B. Molina, Synthesis and characterization of PILCs with single and mix oxide pillars prepared from two different bentonites. A comparative study, Microporous Mesoporous Mater. 29 (1999) 267–281.
[29] F. González, C. Pesquera, I. Benito, S. Mendioroz, Aluminium-gallium pillared montmorillonite with high thermal stability, J. Chem. Soc. Chem. Commun. (1991) 587–588.
[30] N. Maes, E.F. Vansant, Study of Fe_2O_3-pillared clays synthesized using the trinuclear Fe(III)-acetato complex as pillaring precursor, Microporous Mater. 4 (1995) 43–51.
[31] K.S.W. Sing, D.H. Everett, R.A.W. Haul, L. Moscou, R.A. Pierotti, J. Rouquerol, T. Siemieniewska, Reporting physisorption data for gas/solid interface with special reference to the determination of surface area and porosity, Pure Appl. Chem. 57 (1985) 603–619.
[32] J. Rouquerol, P. Llewellyn, K. Sing, Adsorption by clays, pillared clays, zeolites and aluminophosphates, in: F. Rouquerol, J. Rouquerol, K.S.W. Sing, P. Llewellyn, G. Mauribn (Eds.), Adsorption by Powders, Porous Solids: Principles, Methodology and Applications, 2nd ed., Elsevier/Academic Press, Amsterdam, 2014.
[33] P. Yuan, H. He, F. Bergaya, D. Wu, Q. Zhou, J. Zhu, Synthesis and characterization of delaminated iron-pillared clay with meso-microporous structure, Microporous Mesoporous Mater. 88 (2006) 8–15.
[34] E. Murad, Clays and clay minerals: what can mössbauer spectroscopy do to help understand them, Hyperfine Interact. 117 (1998) 39–70.
[35] S. Mørup, H. Topsøe, Mössbauer studies of thermal excitations in magnetically ordered microcristals, Appl. Phys. 11 (1976) 63–66.
[36] M. Luo, D. Bowden, P. Brimblecombe, Catalytic property of Fe-Al pillared clay for Fenton oxidation of phenol by H_2O_2, Appl. Catal B: Environ. 85 (2009) 201–206.
[37] J.G. Carriazo, E. Guelou, J. Barrault, J.M. Tatibouet, S. Moreno, Catalytic wet peroxide oxidation of phenol over Al–Cu or Al–Fe modified clays, Appl. Clay Sci. 22 (2003) 303–308.
[38] B. Iurascu, I. Siminiceanu, D. Vione, M.A. Vicente, A. Gil, Phenol degradation in water through a heterogeneous photo-Fenton process catalyzed by Fe-treated laponite, Water Res. 43 (2009) 1313–1322.
[39] M. Pimentel, N. Oturan, M. Dezotti, M.A. Oturan, Phenol degradation by advanced electrochemical oxidation process electro-Fenton using a carbon felt cathode, Appl. Catal. B: Environ. 83 (2008) 140–149.
[40] J.A. Zazo, J.A. Casas, A.F. Mohedano, M.A. Gilarranz, J.J. Rodríguez, Chemical pathway and kinetics of phenol oxidation by Fenton's reagent, Environ. Sci. Technol. 39 (2005) 9295–9302.
[41] E. Martin del Campo, R. Romero, G. Roa, E. Peralta-Reyes, J. Espino-Valencia, R. Natividad, Photo-Fenton oxidation of phenolic compounds catalysed by iron-PILC, Fuel 138 (2014) 149–155.
[42] B. Iurascu, I. Siminiceanu, D. Vione, M.A. Vicente, A. Gil, Phenol degradation in water through a heterogeneous photo-Fenton process catalysed by Fe-treated laponite, Water Res. 43 (2009) 1313–1322.